Supplementary Information
Abnormal copper coordination obtained by TiO$_2$ overlayer as a key for enhanced photocatalytic hydrogen generation

Vien-Duong Quach,[a] Maria Chiara Spadaro,[b] Diana Dragoe,[d] Marc Botifoll,[b] Hervé Vezin,[f] Christophe Colbeau-Justin,[a] Franck Dumeignil,[e] Jordi Arbiol,[b,c] Robert Wojcieszak,[e] and Mohamed Nawfal Ghazzal,[a†]

[a] Institut de Chimie Physique, Université Paris-Saclay, CNRS UMR 8000, F-91405 Orsay, France.
[b] Catalan Institute of Nanoscience and Nanotechnology (ICN2), CSIC and BIST, Campus UAB, Bellaterra, ES-08193 Barcelona, Catalonia, Spain.
[c] ICREA, Pg. Lluís Companys 23, ES-08010 Barcelona, Catalonia, Spain.
[d] Institut de Chimie Moléculaire et des Matériaux d'Orsay, Université Paris-Saclay CNRS UMR 8182, F-91405 Orsay, France.
[e] UCCS – Unité de Catalyse et Chimie du Solide, Université de Lille, CNRS UMR 8181, F-59000 Lille, France
[f] LASIRE– Laboratoire avancé de spectroscopie pour les interactions la réactivité et l'environnement, Université de Lille, CNRS UMR 8516, F-59000 Lille, France

[†] Corresponding author : mohamed-nawfal.ghazzal@universite-paris-saclay.fr

Materials

Tetraethyl orthosilicate (TEOS, Sigma-Aldrich, 98%), titanium (IV) isopropoxide (TTiP, Sigma-Aldrich, 97%), copper(II) chloride dihydrate ($CuCl_2.2H_2O$, Sigma-Aldrich, $\geq$ 99%), terakis (hydroxylmethyl) phosphonium chloride (THPC, Sigma-Aldrich, 80% in H_2O), L-ascorbic acid ($C_6H_8O_6$, Sigma-Aldrich, 99%), 3-aminopropyl-trimethoxy silane (APTMS, Alfa Aesar, 97%), ammonium hydroxide 28% (NH_4OH, Sigma-Aldrich), Tetramethylammonium hydroxide (TAMH, Sigmal-Aldrich), absolute ethanol (EtOH, VWR Chemicals), methanol (MeOH, Honeywell Fluka), Mill-Q water. All chemical reagents were of analytical grade and used without further purification.

Photocatalyst characterization

High-resolution transmission electron microscopy (HRTEM) and scanning transmission electron microscopy – electron energy loss spectroscopy (STEM-EELS) were carried out in a FEI F20 at 200kV. The HRTEM was acquired with a condenser aperture of 100 μm, no objective aperture, spot size 3, and a BM-UltraScan CCD camera. The STEM-EELS was acquired with a condenser aperture of 70 μm, no objective aperture, nominal camera length of 30mm, spot size 6, and Gatan EF-CCD camera. The EELS supporting STEM images were captured from an annular dark field detector (DF4).

Low-energy ion scattering (LEIS) spectroscopy was performed on a Qtac100 spectrometer (IONTOF GmbH) at the Imperial College of London, the United Kingdom. A 3 keV He^+ beam at normal incidence was selected for qualitative surface analysis. The ionic dose per spectrum was first limited to 1 x 10^{15} ions.cm^{-2} for the core-shell samples to complete the surface analysis and the composition of the sub-surface. The data were processed using the SurfaceLab software from the same manufacturer. LEIS signals were decomposed using the experimental lineshapes of reference materials (at 2379 eV for Cu and 2212 eV for Ti) to take the isotopic distribution of each metal into account.

Powder X-ray diffractograms were recorded on an Aeris powder X-ray diffraction (XRD) diffractometer from Malvern Panalytical Corporation. The measurement was operated at 40 kV and 15 mA with a monochromatized Cu Kα radiation (λ = 1.5406 Å) and a linear VANTEC detector. Raw data were analyzed using X'Pert high score plus software.

X-ray photoelectron spectroscopy (XPS) was performed on a K Alpha spectrometer from ThermoFisher, equipped with a monochromate X-ray Source (Al Kα, 1486.7 eV) with a spot size of 400 μm. The hemispherical analyzer was operated in CAE (Constant Analyzer Energy) mode, with a pass energy of 200 eV and, a step of 1 eV for the acquisition of surveys spectra, and a pass energy of 50 eV and 20eV and a step of 0.1 eV for the acquisition of narrow spectra. A "dual beam" flood gun neutralized the charge build-up. Spectra were treated using CasaXPS software. A Shirley-type background subtraction was used, and peak areas were normalized using the Scofield sensitivity factors. The peaks were fitted with mixed Gaussian-Lorentzian line shapes (70% of Gaussian character). The binding energies were calibrated against the Ti $2p_{3/2}$ binding energy set at 458.5 eV, as the carbon signal is weak.

Fourier-transform infrared (FTIR) spectra experiments were carried out on a FTIR spectrometer (Bruker Vertex 70) equipped with a diamond ATR apparatus (PIKEMIRACLE crystal plate diamond/ZnSe) and an MCT detector. All samples were placed on clean ZnSe diamond plate and 100 scans were performed at a spectral resolution of 4 cm^{-1} in the range of 500-4000 cm^{-1}

The optical properties of our photocatalysts were investigated using steady-state UV-visible diffuse reflectance spectroscopy (UV-vis DRS) ranging from 200 nm to 800 nm. The technique was performed on a Cary 5000 UV-Vis-NIR spectrophotometer; therein, $BaSO_4$ referred to zero baseline correction. The bandgap energy values of samples were estimated via the Tauc equation proposed by Tauc *et al.*[1]:

$$(\alpha h\nu)^{\frac{1}{\gamma}} = B(h\nu - E_g)$$

where α is the extinction coefficient, h is Planck's constant, ν is the photons' frequency, B is constant, and E_g is the bandgap energy. The factor γ represents the nature of electron transition in semiconductors; $\gamma = 2$ for indirect transition and $\gamma = 0.5$ for direct transition. TiO_2 is a semiconductor performing indirect transition[2], leading to $\gamma = 2$. To cancel the influence of light scattering on estimating the bandgap energy, we made use of Kubelka-Munk function[3]:

$$F(R) = \frac{(1 - R)^2}{2R}$$

where R is the reflectance used to deduce absorption spectra. Replacing F(R) on the Tauc equation provides an equation:

$$(F(R)hv)^{\frac{1}{\gamma}} = B(hv - E_g)$$

Time-resolved microwave conductivity (TRMC) allows the study of the lifetime and dynamics of charge carriers that are generated at or transferred to the surface of TiO_2 via the change in conductivity (σ) of the sample induced by a pulsed laser. In particular, mobilized charge carriers (e^-/h^+) induce a relative change in the reflected microwave power ($\Delta P(t)/P$). The following expression gives the relation between conductivity and microwave absorption:

$$\Delta P(t)/P = A \, \Delta\sigma(t) = A \, e \, \Sigma i \, \Delta ni(t) \, \mu i$$

in which Δni is the free charge carrier density, μi is the free charge carrier mobility, and A is the sensitivity factor. A TRMC signal would identify two parameters: maximum conductivity value I_{max} and time decay $I(t)$. The maximum intensity determines the concentration of free charge carrier density created during irradiation. At the same time, the decay $I(t)$ corresponds to the trapping, charge carrier recombination, or electron/proton transfer in time t (from the nanosecond to the microsecond timescale). TRMC setup includes a laser source and a microwave source. The laser source is OPO laser (EKSPLA, NT342B), characterized by the emission of wavelengths from 225 to 2000 nm, with a half-height pulse width of 8 ns and a pulse repetition rate of 10 Hz. Continuously generated microwaves of 30 GHz frequency are derived from a Gunn GKa-300 diode.

Time-resolved laser scanning time-correlated single photon counting (TCSPC) spectroscopy was carried out with a homemade setup based on a TE2000 Nikon microscope equipped with a 60×1.2 NA water immersion objective. The pulsed excitation source was a 375 nm pulsed diode (80 ps FWHM, 20 MHz of repetition rate, PicoQuant). The emitted luminescence was selected with the appropriate filter (420 ± 30 nm) and detected by a MCP-PMT (Hamamatsu), which is connected to the PicoHarp 300 TCSPC module (PicoQuant). Lifetime measurements were analyzed by the Pico-quant SymPhoTime64 software (v5.3.2)

For external quantum efficiency (IPCE) and internal quantum efficiency (APCE) measurements, photoelectrodes were subjected to monochromatic light at various wavelengths triggered from a 1000 W Xe Arc lamp passing through Czerny-Turner monochromators (Quantum Design, MSH-300). The sequence at each wavelength was 10 s dark and 10 s illumination, and the current was collected at 10 points/second. The photoelectrochemical setup remains unchanged, and the bias is at 0.6 V vs. Ag/AgCl (1.23 V vs. RHE). IPCE corresponds to the ratio of photocurrent (electron rate) versus the rate of incident photons:

$$IPCE(\lambda) = \frac{electrons/cm^2/s}{photons/cm^2/s} = \frac{|j_{ph}(mA/cm^2)| \times 1239.8(V \times nm)}{P_{mono}(mW/cm^2) \times \lambda(nm)}$$

APCE describes the photocurrent collected per incident photon absorbed:

$$APCE\ (\lambda) = \frac{IPCE(\lambda)}{1 - 10^{-A}}$$

in which j_{ph} is photocurrent, P_{mono} is the monochromated illumination power intensity, λ is the wavelength at which this illumination power is measured, and A is absorbance from Beer-Lambert law. Experiments were manipulated by potentiostat PGSTAT101 Metrohm Autolab. An open-circuit voltage decay fitting was executed using the inverse method on Matlab. When the numeric curves and the experimental curves show superimposition, the fitting is reliable for estimating important parameters such as the recombination rate constant.

Photocatalytic assessment

We followed a derivatization method[4], which is based on the trace detection of the complex between 2,4-dinitrophenylhydrazine (DNPH) and analytes containing carbonyl group (-C=O) as follows:


DNPH   Carbonyls   DNPH-derivatives
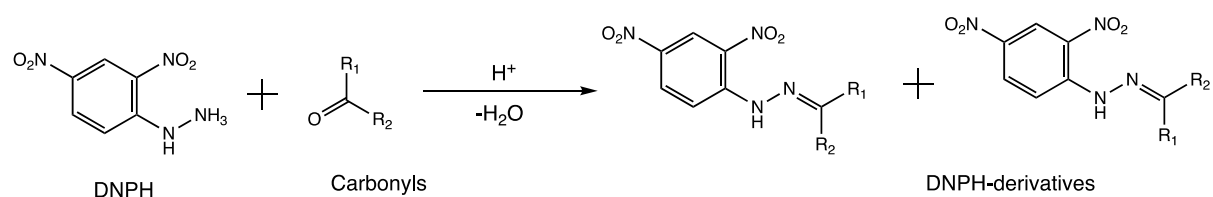
Acetonitrile (CH_3CN) and deionized water (H_2O) (60:40, correspondingly) were used in a reverse-phase analytical column as the eluent. Signals were recorded by a UV-visible detector at a wavelength of 360 nm.
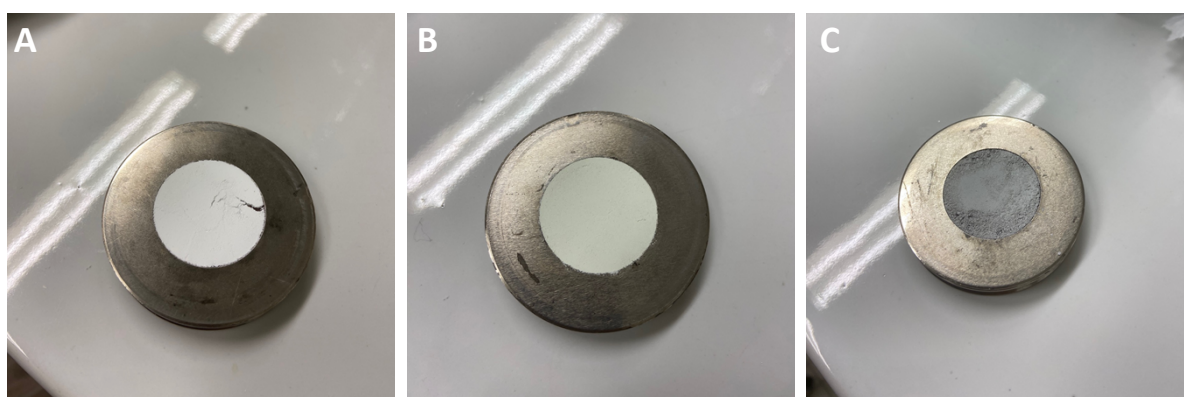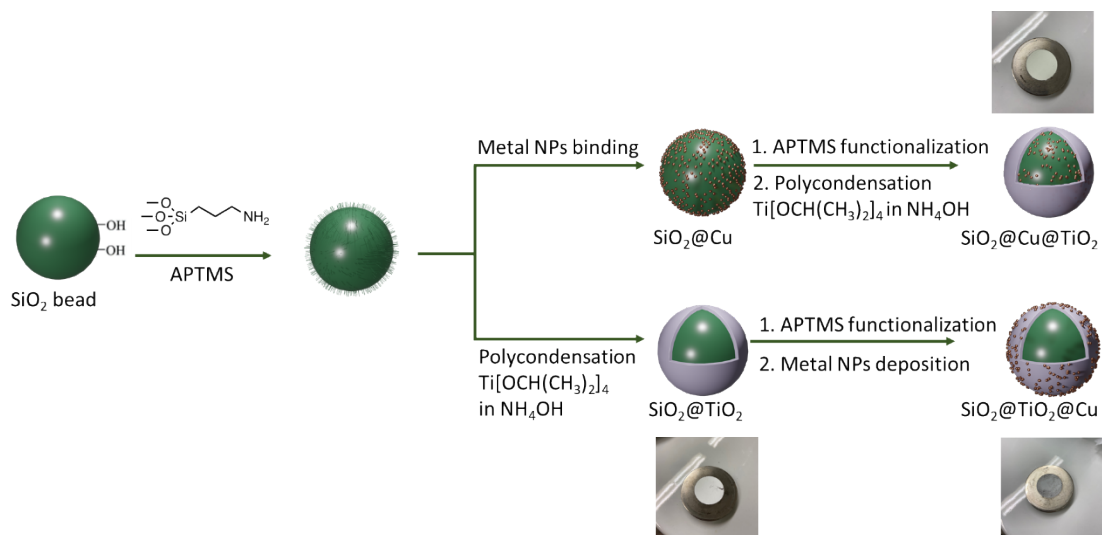
Figure. S1|Schematic illustration of the photocatalysts' soft-chemistry synthesis procedures and visual images: **(A)** $SiO_2@TiO_2$. **(B)** MSI-Cu/TiO_2. **(C)** TiO_2/Cu
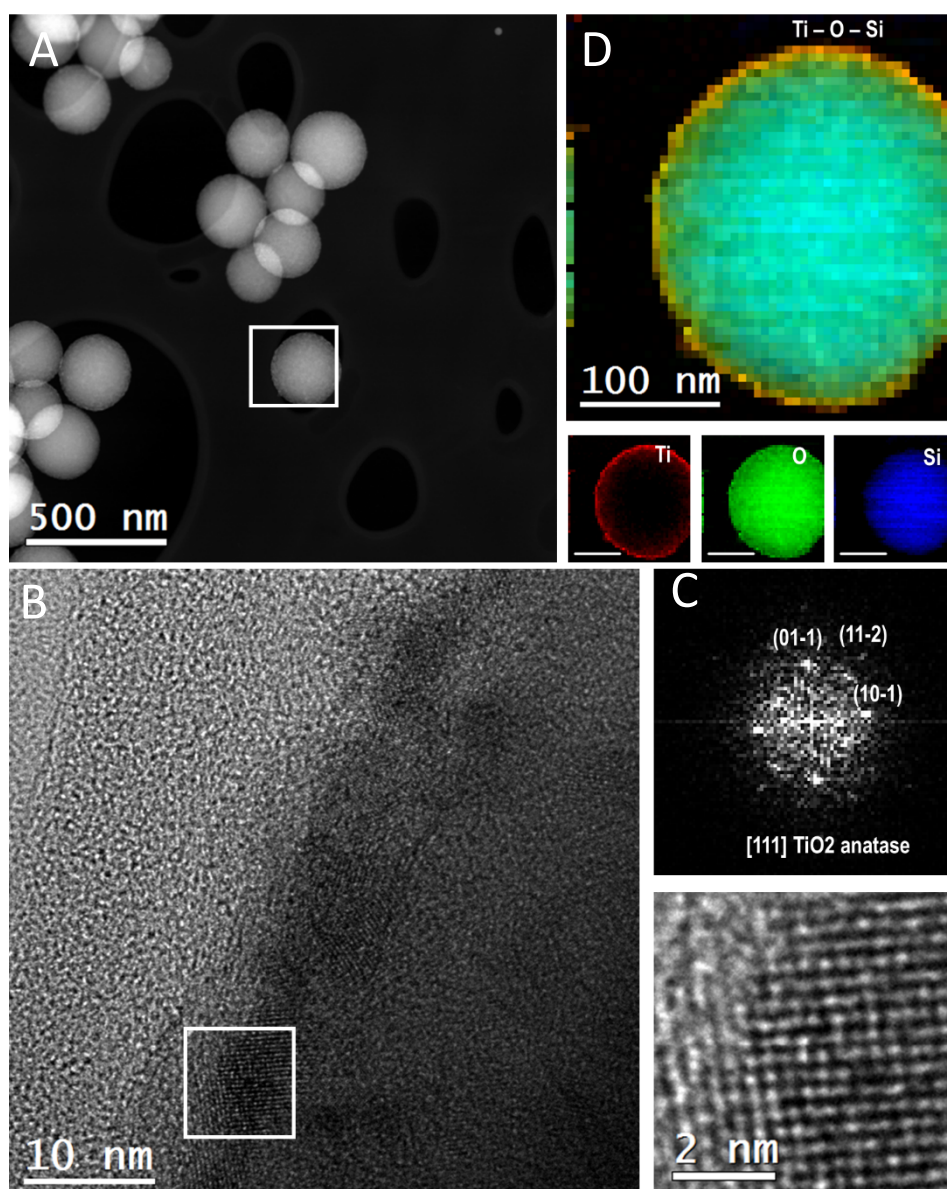
Figure. S2| Electron Microscopy characterization of SiO$_2$@TiO$_2$. **(A)** HAADF-STEM image of the core@shell nanostructure. **(B)** HRTEM image of the TiO$_2$ thin shell. **(C)** High magnification HRTEM image emphasizing TiO$_2$ crystal structure and its index power spectrum. **(D)** EELS-STEM mapping of chemical elements and their composition: Ti L edge at 456 eV (scarlet red), O K edge at 532 eV (kelly green), and Si K edge at 1839 eV (ultramarine blue).
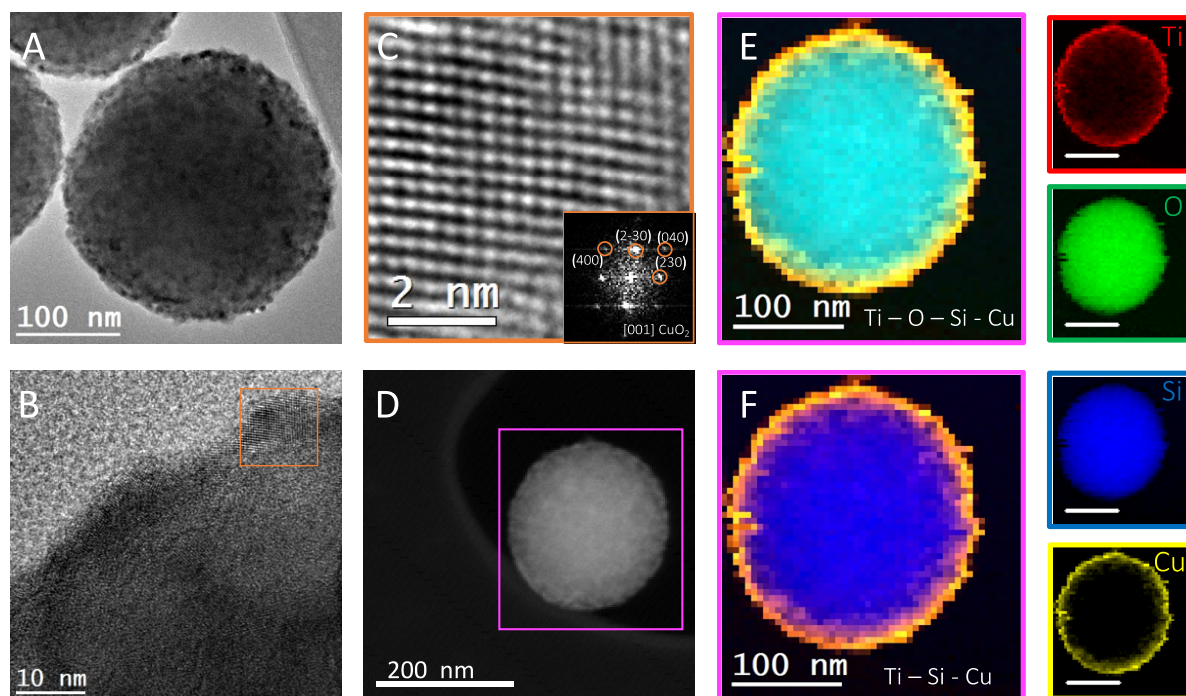
Figure. S3| Electron Microscopy characterization of the TiO$_2$/Cu core@shell photocatalyst. **(A)** TEM image of TiO$_2$/Cu. **(B)** HRTEM image of the interface titania-cuprate. **(C)** High magnification HRTEM image emphasizing a deposited cuprate nanoparticle and its index power spectrum (inlet). **(D)** HAADF-STEM image of a core@shell nanostructure. **(E)-(F)** EELS-STEM mapping of chemical elements and their composition: Ti L edge at 456 eV (scarlet red), O K edge at 532 eV (kelly green), Cu L edge at 931 eV (lemon yellow), and Si K edge at 1839 eV (ultramarine blue).
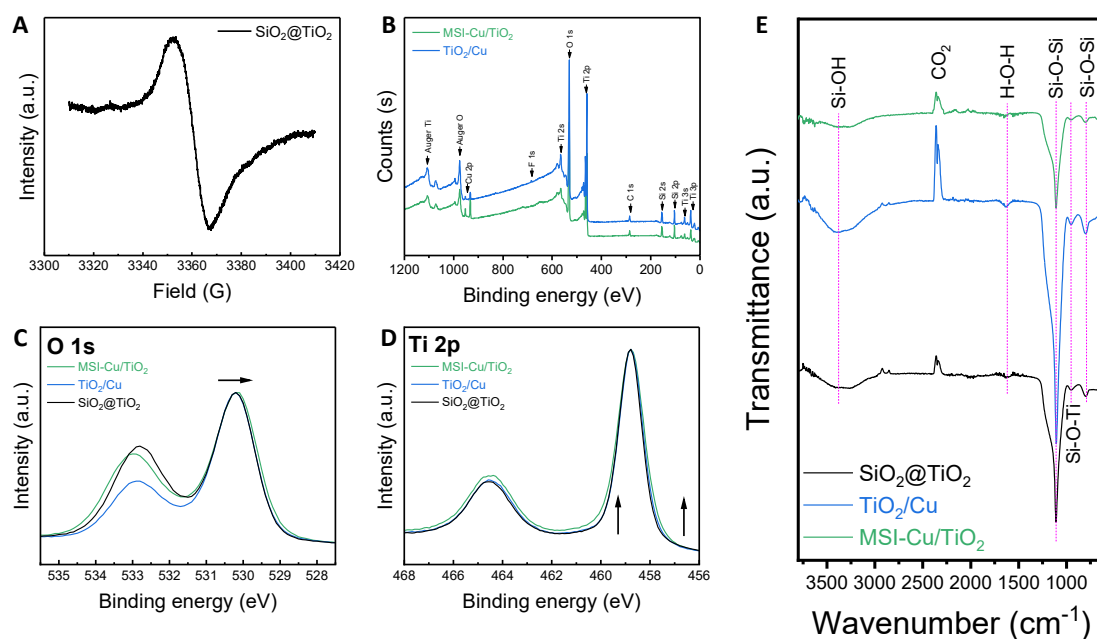
Figure. S4| (A) EPR spectrum of $SiO_2@TiO_2$. **(B)** the survey scans XPS spectra of MSI-Cu/TiO_2 and TiO_2/Cu. Comparison of XPS spectra **(C)** Ti 2p and **(D)** O 1s among MSI-Cu/TiO_2, TiO_2/Cu, and $SiO_2@TiO_2$. **(E)** FTIR spectra.
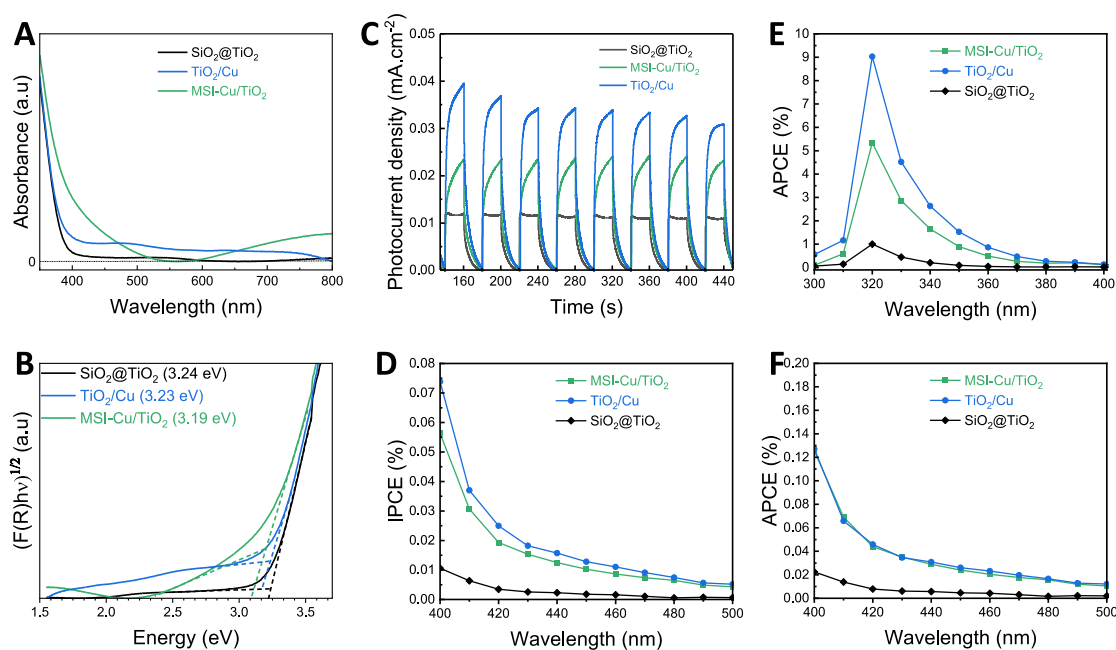
Figure. S5| Optical and photoelectrochemical properties of $SiO_2@TiO_2$, MSI-Cu/TiO_2, and TiO_2/Cu. **(A)** UV-Vis absorption spectra in the 350-800 nm range. **(B)** Tauc plots and bandgap values. **(C)** Amperometric photocurrent response of the photoelectrodes. **(D)** Incident photon-to-current efficiency (IPCE) spectra in the visible range. **(E)** Absorbed photon-to-current efficiency (APCE) spectra in the ultraviolet range. **(F)** Absorbed photon-to-current efficiency (APCE) spectra in the visible range. Photoelectrochemical measurements ran at a fixed bias voltage of 0.6 V vs. Ag/AgCl in saturated KCl ($\sim$ 1.23 V vs. RHE) in Na_2SO_3 0.1 M buffered at pH = 7 under intermittent illumination triggered from a solar simulator AM 1.5G.
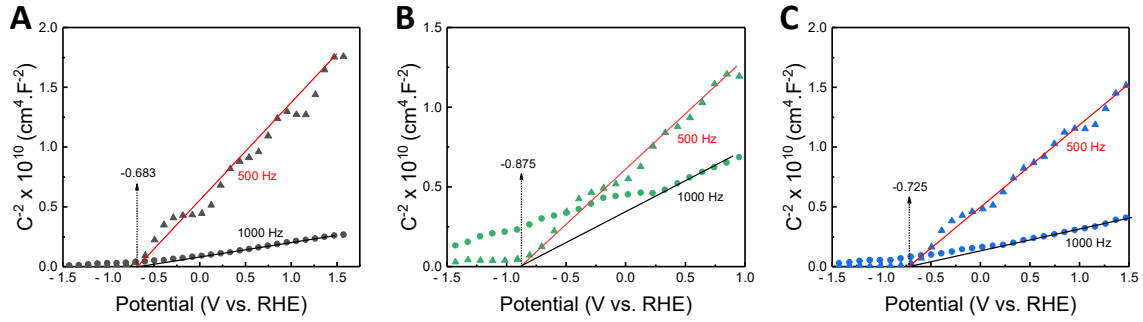
Figure. S6| Mott-Schottky measurement estimating flatband potential values in K_2SO_4 0.5M (pH = 6.32) at a frequency of
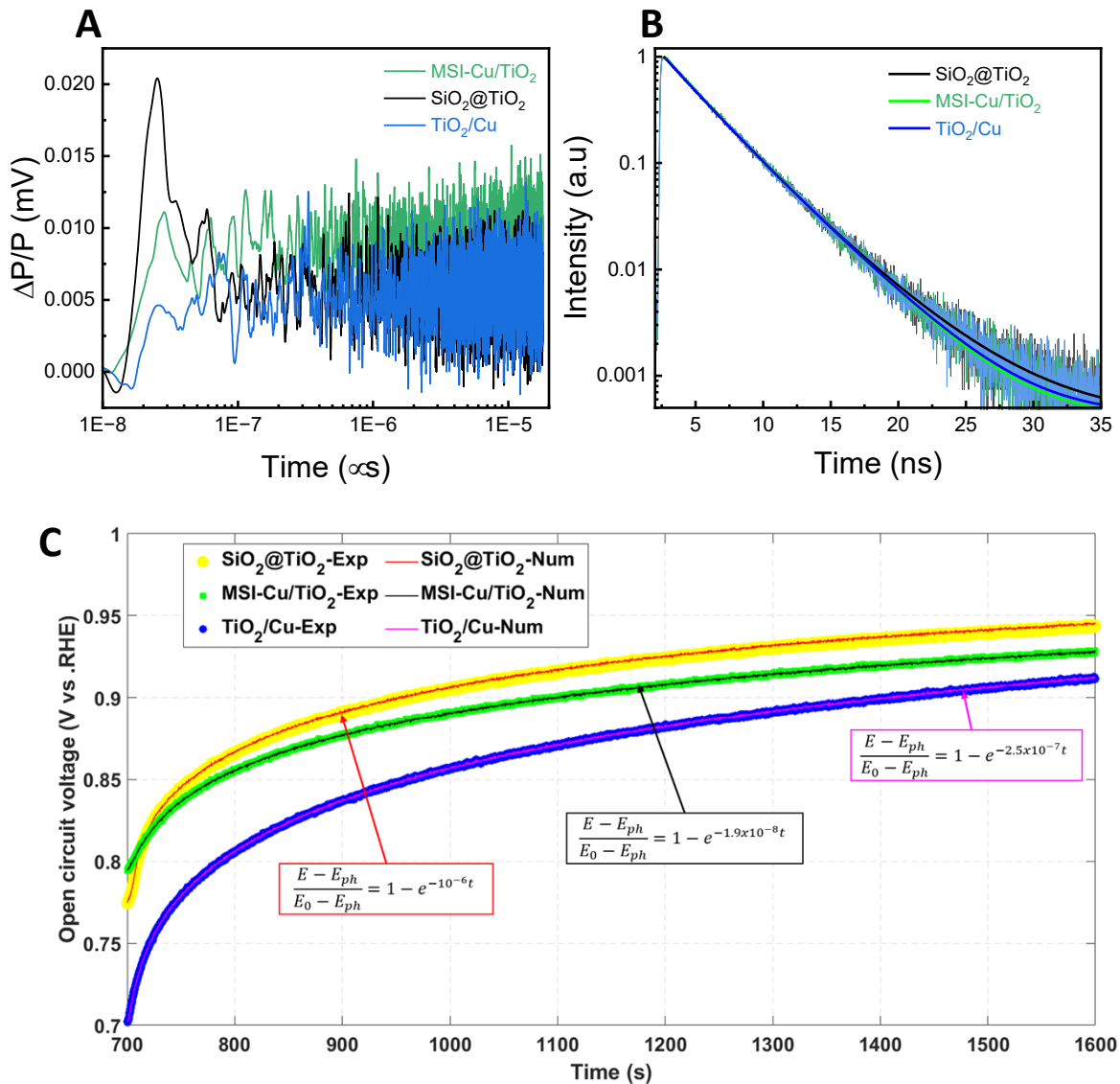
either 1000 Hz or 500 Hz and AC amplitude of 10 mV. **(A)** $SiO_2@TiO_2$. **(B)** MSI-Cu/TiO_2. **(C)** TiO_2/Cu.

Figure. S7|Charge carrier dynamics of $SiO_2@TiO_2$, MSI-Cu/TiO_2, and TiO_2/Cu: **(A)** Time-resolved Microwave Conductivity (TRMC) signals of the samples triggered by laser irradiation (I_{ex}= 1.126 $mJ.cm^{-2}$ at $\lambda = 360\ nm$). **(B)** Time-resolved photoluminescence lifetime decay. **(C)** Open-circuit voltage decay fitting to pseudo-first order kinetic model by Matlab inversed method, estimating recombination rate constants k_r.
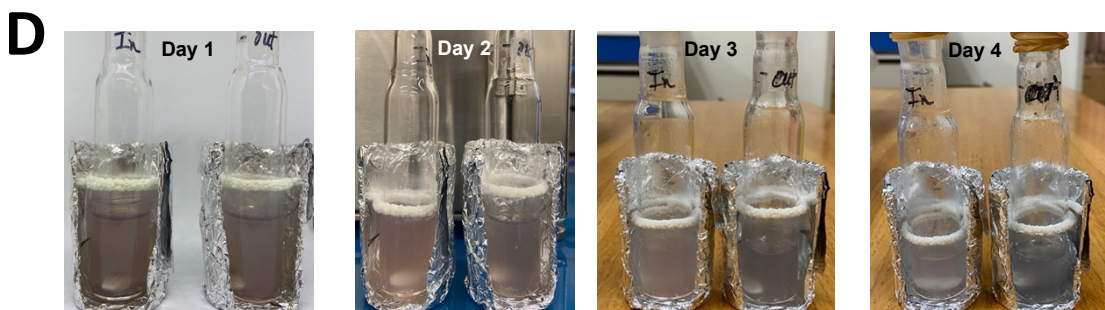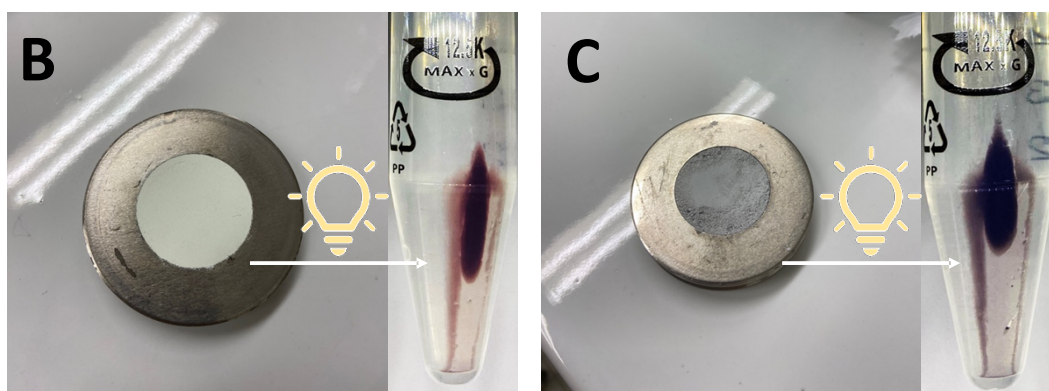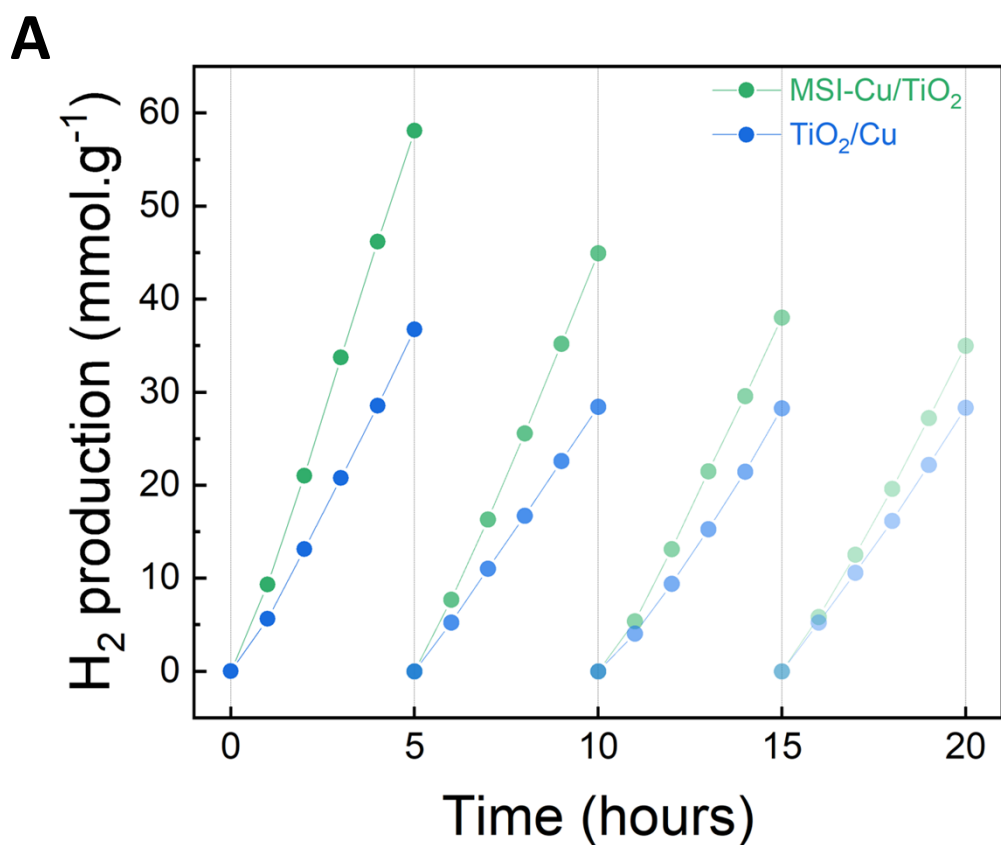
Figure S8| Stability assessment of photocatalytic hydrogen evolution: **(A)** Photocatalytic HER yields of MSI-Cu/TiO$_2$ and TiO$_2$/Cu after 4 cycles of 20 hours. The sample color before and after exposition to UV-Vis irradiation: **(B)** MSI-Cu/TiO$_2$ (greenish), **(C)** TiO$_2$/Cu (grey). **(D)** 37-mL quart reactors containing photocatalysts homogeneously dispersed in aqueous methanol solution during each cycle.

Table S1|Comparision of photocatalytic activity in hydrogen production on recent TiO_2-based photocatalysts.

Photocatalyst	Cu loading	Reaction solution	$m_{photocatalyst}/V_{solution}$	Incident light (light intensity)	Hydrogen evolution rate (mmol/g/h)	Ref.
CuO_x/TiO_2-{0 0 1} (nanosheet)	1.2% wt	MeOH 1:4 (v/v)	50 mg/120 mL	Simulated solar light 1 sun	0.62	[5]
CuO/Cu-TiO_2 (Nanofibers)	1%	MeOH 1:3 (v/v)	100 mg/40 mL	300 W Xenon lamp	0.55	[6]
CuO_x-TiO_2	1%	MeOH 1:3 (v/v)	20 mg/40 mL	Simulated solar light 1 sun	0.40	[7]
Cu_2O/TiO_2 composites	1%	MeOH 1:16 (v/v)	300 mg/300 mL	125W high-pressure Hg lamp	0.84	[8]
Cu-TiO_2 nanofiber/g-C_3N_4	1%	TEOA 1:5 (v/v)	20 mg/ 150 mL	300 W Xenon lamp	0.26	[9]
Doughnut-shaped black TiO_2/Cu/ZnO	N/A	TEOA 1:9 (v/v)	50 mg/ 100 mL	300 W Xeon lamp, 420 nm cut-off filter	0.34	[10]
CuO/WO_3	17.87%	Pure MeOH	100 mg/ 10 mL	Visible light irradiation	0.019	[11]
Cu_2O/TiO_2	0.50%	MeOH 1:9 (v/v)	100 mg/ 80 mL	150 W Xenon lamp	0.36	[12]
$Cu_2O/ZrTiO_4$	0.50%	MeOH 1:9 (v/v)	100 mg/ 80 mL	150 W Xenon lamp	0.06	[12]
Z-Scheme (001)-faceted TiO_2/Cu_2O	1.4% wt Cu_2O	MeOH 1:9 (v/v)	20 mg/ 100 mL	300 W Xenon lamp	0.75	[13]
single-atom Cu/TiO_2	0.75% wt Cu	MeOH 1:3 (v/v)	5 mg/ 80 mL	300W Xe lamp (100W/m2)	16.6	[14]
Cu_2O/TiO_2 nanorod	1% wt Cu_2O	MeOH 1:4 (v/v)	100 mg/ 80 mL	300W Xe lamp (80W/m2)	1.52	[15]
Cu^{+1}/Cu^0-TiO_2 mesoporous nanocomposite	3% wt Cu	MeOH 1:4 (v/v)	30 mg/ 5 mL	Direct sunlight (637W/m2)	0.17	[16]
TiO_2-Cu nanowire	N/A	MeOH 1:3 (v/v)	50 mg/ 80 mL	4 x 3W UV-LED (365 nm, 80 W/m2)	5.1	[17]
Cu NPs/TiO_2 P25	18.90% wt Cu	MeOH 1:9 (v/v)	25 mg/ 25 mL	300 W Xenon lamp	0.07	[18]
Cu-loaded TiO_2 P25	9% wt	MeOH 1:9 (v/v) in tap water	40 mg/ 40 mL	300 W Xe lamp	12.7	[19]
$Cu_2O/CuO/TiO_2$	0.5% mol Cu	MeOH 1:4 (v/v)	100 mg/ 100 mL	300 W Xe lamp	0.113	[20]
CuO@TiO_2	16.54% wt CuO	TEOA 15%, 20 mg of eosin Y (photosensitizer)	20 mg/ 80 mL	300 W Xenon lamp (cutoff λ < 420 nm)	1.46	[21]
Cu_2O–TiO_2 nanofiber	12.04% wt CuO	MeOH 1:25 (v/v)	20 mg/ 50 mL	200-W Hg lamp	0.048	[22]
Cu_7S_4-enwrapped Cu_2O	N/A	Na_2SO_3 0.5M	10 mg/ 100 mL	300 W Xe lamp	1.69	[23]
MSI-Cu/TiO_2	**1% wt**	**MeOH 1:3 (v/v)**	**10 mg/ 10 mL**	**150 W Hg lamp**	**11.82**	**This work**

1 J. Tauc, R. Grigorovici and A. Vancu, *physica status solidi (b)*, 1966, **15**, 627–637.

2 D. Reyes-Coronado, G. Rodríguez-Gattorno, M. E. Espinosa-Pesqueira, C. Cab, R. de Coss and G. Oskam, *Nanotechnology*, 2008, **19**, 145605.

3 P. Kubelka and F. Munk, *A Contribution to the Optics of Pigments*, Z. Technol. Phys, 1931.

4 A. Soman, Y. Qiu and L. Q. Chan, *Journal of Chromatographic Science*, 2008, **46**, 461–465.

5 Y. Liu, Z. Ye, D. Li, M. Wang, Y. Zhang and W. Huang, *Applied Surface Science*, 2019, **473**, 500–510.

6 H. Hou, M. Shang, F. Gao, L. Wang, Q. Liu, J. Zheng, Z. Yang and W. Yang, *ACS Applied Materials & Interfaces*, 2016, **8**, 20128–20137.

7 P. A. Bharad, A. V. Nikam, F. Thomas and C. S. Gopinath, *ChemistrySelect*, 2018, **3**, 12022–12030.

8   M. Muscetta, S. A. Jitan, G. Palmisano, R. Andreozzi, R. Marotta, S. Cimino and I. Di Somma, *Journal of Environmental Chemical Engineering*, 2022, **10**, 107735.

9   H. Khan, H. Charles and C. S. Lee, *Applied Surface Science*, 2023, **607**, 155068.

10 B. Chen, J. Zhang, J. Yu, R. wang, B. He, J. Jin, H. Wang and Y. Gong, *Journal of Colloid and Interface Science*, 2022, **607**, 760–768.

11 H. Wang, M. Xiao, Z. Wang, X. Chen, W. Dai and X. Fu, *Chemical Engineering Journal*, 2023, **459**, 141616.

12 V. Polliotto, S. Livraghi, A. Krukowska, M. V. Dozzi, A. Zaleska-Medynska, E. Selli and E. Giamello, *ACS Applied Materials & Interfaces*, 2018, **10**, 27745–27756.

13 T. Wei, Y. N. Zhu, X. An, L. M. Liu, X. Cao, H. Liu and J. Qu, *ACS Catalysis*, 2019, **9**, 8346–8354.

14 B. H. Lee, S. Park, M. Kim, A. K. Sinha, S. C. Lee, E. Jung, W. J. Chang, K. S. Lee, J. H. Kim, S. P. Cho, H. Kim, K. T. Nam and T. Hyeon, *Nature Materials*, 2019, **18**, 620–626.

15 Y. Liu, B. Zhang, L. Luo, X. Chen, Z. Wang, E. Wu, D. Su and W. Huang, *Angewandte Chemie - International Edition*, 2015, **54**, 15260–15265.

16 R. A. Rather, S. Singh and B. Pal, *Journal of Catalysis*, 2017, **346**, 1–9.

17 S. Xiao, P. Liu, W. Zhu, G. Li, D. Zhang and H. Li, *Nano Letters*, 2015, **15**, 4853–4858.

18 H. Tian, X. L. Zhang, J. Scott, C. Ng and R. Amal, *Journal of Materials Chemistry A*, 2014, **2**, 6432–6438.

19 W. J. Foo, C. Zhang and G. W. Ho, *Nanoscale*, 2013, **5**, 759–764.

20 F. Yang, M. Liu, X. Chen, Z. Xu and H. Zhao, *Solar RRL*, , DOI:10.1002/solr.201870234.

21 Y. S. Ouyang, S. T. Zheng, G. W. Guan and Q. Y. Yang, *ACS Applied Energy Materials*, 2022, **5**, 14455–14465.

22 K. Sekar, C. Chuaicham, B. Vellaichamy, W. Li, W. Zhuang, X. Lu, B. Ohtani and K. Sasaki, *Applied Catalysis B: Environmental*, , DOI:10.1016/j.apcatb.2021.120221.

23 M. Zhang, Z. Chen, Y. Wang, J. Zhang, X. Zheng, D. Rao, X. Han, C. Zhong, W. Hu and Y. Deng, *Applied Catalysis B: Environmental*, 2019, **246**, 202–210.